Broadband infrared binary-pattern metasurface absorbers with micro-genetic algorithm optimization

Zhigang Li,[1] Liliana Stan,[2] David A. Czaplewski,[2] Xiaodong Yang,[1,3] and Jie Gao[1,*]

[1]*Department of Mechanical and Aerospace Engineering, Missouri University of Science and Technology, Rolla, Missouri 65409, USA*
[2]*Center for Nanoscale Materials, Argonne National Laboratory, Argonne, Illinois 60439, USA*
[3]*e-mail: yangxia@mst.edu*
Corresponding author: gaojie@mst.edu

Broadband binary-pattern metasurface absorbers are designed and demonstrated in the mid-infrared wavelength range through the micro-genetic algorithm. The tungsten-based metasurface absorbers with the optimized binary-pattern nanostructures exhibit broadband near-perfect absorption due to the multiple plasmonic resonances supported within the unit cell. Furthermore, the influence of minor pixel modifications in the optimized binary-pattern nanostructures on the absorption performance is investigated in the experiment. This Letter presents a promising approach to design and optimize complex optical nanostructures with the desired properties for metamaterial and metasurface applications. © 2018 Optical Society of America

https://doi.org/10.1364/OL.44.000114

Electromagnetic metamaterial absorbers have been receiving great interest since the first demonstration of the perfect absorption properties [1]. Metamaterial absorbers have been designed to realize broadband or narrowband absorption at wavelengths from visible to infrared [2]. Various geometries have been used to design broadband metamaterial absorbers, mainly including multilayer films based on an impedance match theory [3], metal-dielectric-metal structures with multiple resonators [4], structured multilayer gratings [5], and hybrid structures with multiple absorption mechanisms [6]. These metamaterial absorbers are constrained by the manual design process with limited geometry complexity and tedious parameters sweeping. Several optimization methods have been proposed to simplify the nanostructure design, including gradient-based methods [7], evolutionary models such as genetic algorithms [8–10], particle swarm optimization [11], and non-deterministic quasi-random methods [12]. Genetic algorithms have been proved to be an efficient approach for the absorber design [8–10,13]. Starting from one random distribution of materials selection, the genetic algorithm searches the optimal distribution through the steps in the crossover of parents' information, evaluating the offspring's information, and

repeating the loop over until reaching the stop criteria. Furthermore, a micro-genetic algorithm (micro-GA) is a modified genetic algorithm by adding the option of restarting the initialization of population, which requires a smaller initial population and converges faster than the traditional genetic algorithm [8].

In this Letter, a micro-GA is employed to design the broadband mid-infrared binary-pattern metasurface absorbers. The tungsten-based structure is selected for the optimization towards broadband near-perfect absorption. The optimized binary-pattern nanostructures within the unit cell support multiple plasmonic resonances to achieve broadband absorption. The effects of minor pixel modifications in the optimized nanostructures on the absorption performance are further investigated. This Letter provides an effective way to optimize complex metamaterial and metasurface nanostructures with the desired properties.

In the micro-GA, the binary-pattern nanostructure is encoded into the chromosome with binary numbers defined as either material ("1") or free space ("0"). To enable the evolutionary optimization toward the optimal result, the fitness function is defined as $F = \sum_\theta \sum_\lambda (1 - A_{\mathrm{TM}})^2 + (1 - A_{\mathrm{TE}})^2$ to evaluate the absorption property for each binary-pattern nanostructure, where A_{TM} and A_{TE} are the absorption under TM and TE polarization, respectively, at a certain incident angle θ. Thus, the design problem of a binary-pattern nanostructure is formulated as the minimization of the fitness function F subject to $\nabla \times \nabla \times \boldsymbol{E} - \mu\omega^2\epsilon\boldsymbol{E} = 0$ and $\nabla \cdot \epsilon\boldsymbol{E} = 0$, where $\boldsymbol{E}$, ϵ, and μ denote the electric field, permittivity, and permeability, respectively, in the unit cell. Periodic boundary conditions are applied around the unit cell in simulation using COMSOL software. The fitness value F is then extracted from the simulated absorption spectra for each obtained binary-pattern nanostructure, and it is further evaluated to stop or start new calculation loops according to the criteria conditions.

The optimization target is to obtain the absorption above 0.9 at the selected 12 equally spaced wavelengths from 2 to 4 μm at two incident angles of 0° and 45°. The binary-pattern nanostructure is encoded with an 11 by 11 array with "1s" and
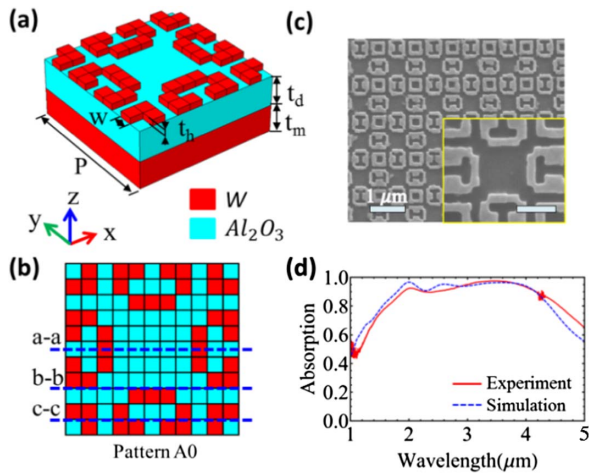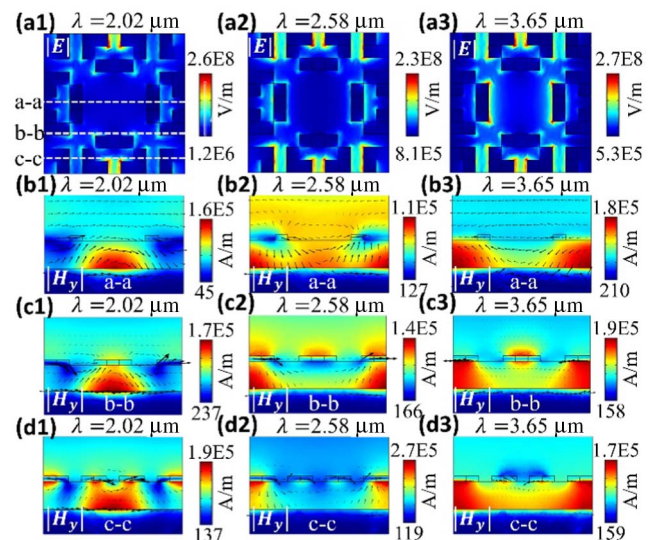
Fig. 1. (a) and (b) Schematic of the optimized binary-pattern A0 in the unit cell and top view. (c) SEM images of the pattern A0 array. Insert image scale bar: 400 nm. (d) Measured and simulated broadband absorption from the pattern A0 array under unpolarized normal incidence.


Fig. 2. (a1)–(a3) Top view of the electric field $|E|$ distributions at the top W surface of pattern A0 at $\lambda = 2.02$, 2.58, and 3.65 μm. Cross-sectional view of the magnetic field $|H_y|$ distributions at the locations of (b1)–(b3) a-a, (c1)–(c3) b-b, and (d1)–(d3) c-c under TM polarization at normal incidence. The black arrows depict the direction and magnitude of the induced electric current density.

"0s," respectively, where the eight-fold mirror symmetry is applied to enable polarization independence and to shorten the chromosome string. Due to the advantages of the micro-GA in searching solutions, a population of five chromosomes is used with the tournament selection for crossover [8–10]. No mutation step is required, since the repopulation step after reaching a value of the similarity among chromosomes will significantly accelerate the evolution progress. The two optimized patterns presented in this Letter start from random structures initially and converge to the fitness values satisfying the design target within 35 generations.

Figure 1(a) shows the schematic of the optimized binary-pattern nanostructure pattern A0 in the unit cell through the micro-GA, with the top view shown in Fig. 1(b), where the dashed blue lines mark the cross-sectional locations for optical field analysis in Fig. 2. The multilayer is composed of a top 45 nm thick tungsten (W) layer, a 220 nm thick alumina (Al_2O_3) spacer layer, and a 200 nm thick tungsten ground plane on a silicon substrate, denoted as t_h, t_d, and t_m, respectively. Tungsten is used for its high intrinsic loss and high temperature enduring ability, giving it the potential for thermal absorber and emitter design [4]. The pattern A0 in the unit cell is made of an 11 by 11 square pixel array filled with either W or air based on the optimization result with a pixel width w of 100 nm. The tungsten ground plane is thick enough to effectively block the transmission so that the absorption is calculated as unity minus the reflection.

The W-Al_2O_3-W multilayer stack was deposited on a silicon substrate by RF sputtering. Both W and Al_2O_3 were grown in an Ar atmosphere at 6.5 and 5 mTorr, respectively. The deposition rates were 0.75 Å/s for W and 0.08 Å/s for Al_2O_3. The designed binary-pattern nanostructure was then fabricated with focused ion beam (FIB) milling on the top tungsten layer. Figure 1(c) shows a scanning electron microscopy (SEM) image of the fabricated pattern A0 array. Variations in the FIB milling process cause the 100 nm pixels to vary by ±8 nm. The unpolarized reflection spectrum is measured at normal incidence with Fourier transform infrared spectroscopy. The measured absorption spectrum for the fabricated pattern A0 array is plotted in Fig. 1(d), showing that broadband near-perfect absorption is obtained with the absorption over 0.9 from 1.9 to 4.2 μm and over 0.95 from 3 to 3.9 μm. The simulated absorption spectrum with the averaged polarization matches the experimental data well where, in simulation, the permittivity parameters of W and Al_2O_3 are taken from Rakic et al. [14] and Kischkat et al. [15], respectively.

In order to understand the mechanism of broadband absorption for the optimized pattern A0, optical mode analysis is conducted at the three resonance wavelengths ($\lambda = 2.02$, 2.58, and 3.65 μm), as shown in Fig. 2. Figures 2(a1)–2(a3) show the top view of the electric field $|E|$ distributions at the top W surface with normal incidence under TM polarization. It shows that the electric field distributions are enhanced at certain locations of the nanostructure at different resonance wavelengths. These multiple plasmonic resonances are also observed from the magnetic field $|H_y|$ distributions in Figs. 2(b1)–2(b3), Figs. 2(c1)–2(c3), and Figs. 2(d1)–2(d3) at the cross sections of a-a, b-b, and c-c, respectively. The black arrows plotted in the magnetic fields describe the direction and magnitude of the induced electric current density.

Figure 2(b1) presents a loop of the induced electric current between the top W layer and the W ground plane, which is a signature of magnetic resonance resulting from the antiparallel currents [1,4]. These current loops are also observed in other cross sections, but with different distributions due to the certain pixel arrangement at each cross section. The multiple plasmonic resonances supported in the binary-pattern nanostructure are responsible for the achieved near-perfect broadband absorption. Additionally, as tungsten is treated as a non-magnetic dispersive medium in the designed metasurface absorber, the time-averaged dissipative power density reads
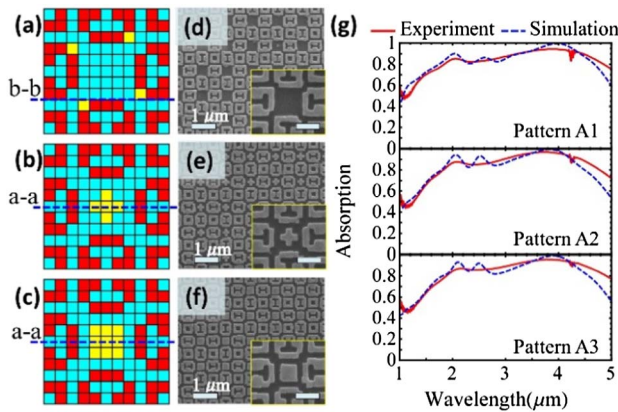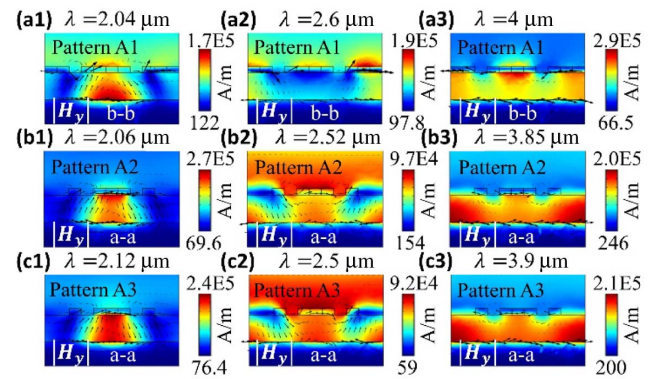
Fig. 3. (a)–(c) Schematic of three types of modified patterns A1, A2, and A3 with yellow pixels representing the perturbations to pattern A0. (d)–(f) SEM images of patterns A1, A2, and A3. Scale bar: 400 nm. (g) Measured and simulated absorption spectra under unpolarized normal incidence.

Fig. 4. Cross-sectional view of the magnetic field $|H_y|$ distributions of (a1)–(a3) pattern A1 at the location b-b, (b1)–(b3) pattern A2 at the location a-a, and (c1)–(c3) pattern A3 at the location a-a at three resonance wavelengths under TM polarization at normal incidence.

$Q_h = \frac{\epsilon_0 \omega \epsilon_m''(\omega)|E|^2}{2}$, where ϵ_m'' denotes the imaginary part of the permittivity [16]. It indicates that the absorbed electromagnetic energy is finally converted to heat dissipation due to the optical loss in tungsten.

In order to investigate the dependence of the absorption performance on the minor pixel modifications of the optimized binary-pattern nanostructure, three types of nanostructures are designed: patterns A1, A2, and A3, as shown in Figs. 3(a)–3(c), respectively, in the 11 by 11 square pixel arrays with a pixel width of 100 nm. The yellow pixels are the intentionally added tungsten pixels to introduce the perturbation to the originally optimized nanostructure pattern A0. In Fig. 3(a), for pattern A1, four yellow pixels are placed at the corners of the nanostructure in the clockwise direction which breaks the central mirror symmetry of pattern A0, and the SEM image is shown in Fig. 3(d). The broken symmetry is expected to lead to significant influence on the absorption spectra. The measured and simulated absorption spectra of pattern A1 are plotted in Fig. 3(g), showing that the three resonance wavelengths are redshifted to $\lambda = 2.04$, 2.6, and 4 µm, respectively, and the absorption values are lower in the wavelength range from 2 to 3.5 µm compared to pattern A0. Furthermore, Figs. 3(b) and 3(c) present the perturbed patterns A2 and A3 with the additional central cross and square structures, respectively. The corresponding absorption spectra of patterns A2 and A3, shown in Fig. 3(g), exhibit similar behavior due to the same plasmonic resonance mechanism for cross and square structures with the same geometric length and thickness [17]. Compared to pattern A1, the resonances at ~2.5 µm for patterns A2 and A3 are observed to have blueshifts, and the absorption increases slightly at this wavelength due to the central cross/square structure. However, compared to pattern A0, the separations between the two resonances in the wavelength range of 2.5–4 µm become larger and lead to the absorption performance degradation from the optimized pattern A0.

The perturbation of absorption performance can be understood with optical mode analysis for the modified nanostructures. Figure 4 shows the cross-sectional view of the magnetic field $|H_y|$ distributions of patterns A1, A2, and A3 at the locations marked by the dashed blue lines in Figs. 3(a)–3(c). The yellow pixels in pattern A1 are expected to modify the magnetic field distributions, which are verified through simulation results in Figs. 4(a1)–4(a3) at the b-b cross section. The asymmetric magnetic field distribution on the top metal layer is presented in Fig. 4(a2) due to the existence of the added pixels in pattern A1, compared with the central symmetric magnetic field distribution of pattern A0 shown in Fig. 2(c2). Patterns A2 and A3 keep the same central mirror symmetry as pattern A0 after adding new pixels. In Figs. 4(b1)–4(c3), the magnetic field $|H_y|$ distributions of patterns A2 and A3 at the a-a cross section are similar at three resonance wavelengths, so that it is almost equivalent to add either the central cross structure or the square structure into pattern A0. The observed variations of magnetic field distributions of patterns A2 and A3 compared with those of pattern A0 in Figs. 2(b1)–2(b3) explain the perturbations due to the central structures, which result in the wavelength shifts for the resonances and the lower absorption in the spectra at a wavelength range of 2.5–3.5 µm for patterns A2 and A3.

In theory, there are multiple solutions available for the optimized binary-pattern nanostructures to achieve the broadband near-perfect absorption performance. However, it is difficult to find all the solutions due to the constraints from the optimization algorithm, the practical fabrication limit, and the limited computational resources [8–10,13]. An evolutionary optimization algorithm, for instance the micro-GA, will usually converge to a local minimum under predefined constraints for the target fitness value or just stop with the criteria of a maximum generation number. In this Letter, except pattern A0, another type of nanostructure pattern B0 is also found to satisfy the design target with a constraint condition of 125 nm pixel width. Figure 5(a) shows the top view of pattern B0 in the 11 by 11 array with the pixel width of 125 nm, and Fig. 5(e) gives the SEM image. The measured and simulated absorption spectra are plotted in Fig. 5(k), showing broadband absorption over 0.9 from 1.75 to 4.03 µm or over 0.95 from 2.8 to 3.8 µm. Three resonance peaks at the wavelengths of 1.71, 2.51, and 3.53 µm are found for pattern B0. Similar to pattern A0, the broadband absorption performance of pattern B0 also results from multiple plasmonic resonances.
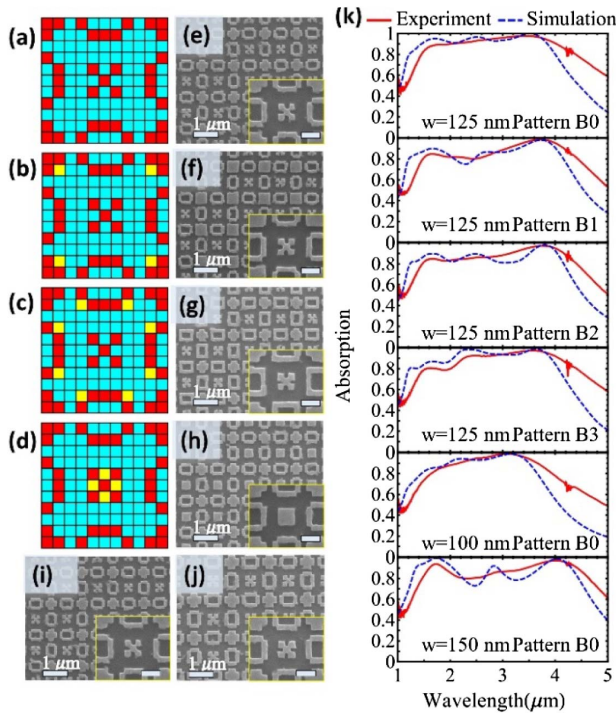
Fig. 5. Schematics of (a) pattern B0 and three modified nanostructures (b) pattern B1, (c) pattern B2, and (d) pattern B3 with the added yellow tungsten pixels. (e)–(h) SEM images of patterns B0, B1, B2, and B3. (i) and (j) SEM images of the scaled nanostructures with pattern B0, but with pixel widths $w = 100$ and 150 nm. Scale bar: 400 nm. (k) Measured and simulated absorption spectra under unpolarized normal incidence for the nanostructures in (e)–(j).

The perturbation of absorption performance due to the minor pixel modifications of pattern B0 is also investigated with the new nanostructures of patterns B1, B2, and B3 with single-pixel level modifications, as shown in Figs. 5(b)–5(d) for schematics and Figs. 5(f)–5(h) for SEM images. The influence from the minor modifications is clearly seen in the absorption spectra in Fig. 5(k). Compared with the absorption spectrum of pattern B0, patterns B1 and B2 exhibit redshifts for the resonance wavelengths and a slightly lower absorption in the wavelength range of 2–3.5 μm, while pattern B3 shows a more significant absorption degradation in the wavelength range of 1.3–2 μm. The observed spectra indicate that the intentionally added single-pixel defects have different levels of impact on the absorption performance according to the certain pixel locations. Furthermore, the scaling effect when designing the nanostructure is another factor to perturb the absorption performance. Here the designed pattern B0 is scaled up and down through adjusting the pixel width w as 100 and 150 nm in the unit cell. The SEM images of the scaled nanostructures are shown in Figs. 5(i) and 5(j), and the corresponding absorption spectra are plotted in the last two panels of Fig. 5(k). With a smaller pixel width of 100 nm, the absorption bandwidth shrinks, and the resonance wavelengths are blueshifted. (For example, a resonance shift from 3.55 to 3.17 μm is observed in the long

wavelength region.) In contrast, with the larger pixel width of 150 nm, the absorption bandwidth is broadened, and the resonance wavelengths show redshifts. However, the absorption from 2 to 3 μm is significantly lowered to below 0.86. In general, the absorption performance is degraded in both cases due to the modification of the optimized nanostructure with the pixel width of 125 nm.

In summary, this Letter presents the micro-GA enabled design optimization for the W-based broadband mid-infrared binary-pattern metasurface absorbers. Two kinds of optimized nanostructures are found to exhibit excellent absorption performance. The broadband absorption properties are contributed from the multiple plasmonic resonances supported in the unit cell. Furthermore, the absorption perturbations due to the minor modifications of the optimized nanostructures by adding extra tungsten pixels are discussed. This Letter provides an effective and efficient approach to design and optimize complex metamaterial and metasurface nanostructures for realizing high-performance functional optical devices.

REFERENCES

1. N. I. Landy, S. Sajuyigbe, J. J. Mock, D. R. Smith, and W. J. Padilla, Phys. Rev. Lett. **100**, 1 (2008).
2. C. M. Watts, X. Liu, and W. J. Padilla, Adv. Mater. **24**, OP98 (2012).
3. H. Deng, Z. Li, L. Stan, D. Rosenmann, and D. Czaplewski, Opt. Lett. **40**, 2592 (2015).
4. H. Wang and L. Wang, Opt. Express **21**, A1078 (2013).
5. Y. Cui, K. H. Fung, J. Xu, H. Ma, Y. Jin, S. He, and N. X. Fang, Nano Lett. **12**, 1443 (2012).
6. M. Desouky, A. M. Mahmoud, and M. A. Swillam, Sci. Rep. **8**, 2036 (2018).
7. B. Vial and Y. Hao, Opt. Express **23**, 23551 (2015).
8. S. Chakravarty, R. Mittra, and N. R. Williams, IEEE Trans. Antennas Propag. **50**, 284 (2002).
9. J. A. Bossard, S. Yun, D. H. Werner, and T. S. Mayer, Opt. Express **17**, 14771 (2009).
10. J. A. Bossard, L. Lin, S. Yun, L. Liu, D. H. Werner, and T. S. Mayer, ACS Nano **8**, 1517 (2014).
11. S. Roy, S. D. Roy, J. Tewary, A. Mahanti, and G. K. Mahanti, Prog. Electromagn. Res. B **62**, 121 (2015).
12. S. Yu, C. Wang, Y. Zhang, B. Dong, Z. Jiang, X. Chen, W. Chen, and C. Sun, Sci. Rep. **7**, 3752 (2017).
13. S. Jafar-Zanjani, S. Inampudi, and H. Mosallaei, Sci. Rep. **8**, 11040 (2018).
14. A. D. Rakić, A. B. Djurišić, J. M. Elazar, and M. L. Majewski, Appl. Opt. **37**, 5271 (1998).
15. J. Kischkat, S. Peters, B. Gruska, M. Semtsiv, M. Chashnikova, M. Klinkmüller, O. Fedosenko, S. Machulik, A. Aleksandrova, G. Monastyrskyi, Y. Flores, and W. Ted Masselink, Appl. Opt. **51**, 6789 (2012).
16. J. Hao, L. Zhou, and M. Qiu, Phys. Rev. B **83**, 165107 (2011).
17. A. Sakurai, B. Zhao, and Z. M. Zhang, J. Quantum Spectrosc. Radiat. Transfer **149**, 33 (2014).